High energy laser pulse self-compression in short gas filled fibers

P. N. Anderson,[1] P. Horak,[1] J. G. Frey,[2] and W. S. Brocklesby[1]

[1] *Optoelectronics Research Centre, Faculty of Physical Sciences and Engineering, University of Southampton, Southampton, United Kingdom, SO17 1BJ*

[2] *Chemistry, Faculty of Natural and Environmental Sciences, University of Southampton, Southampton, United Kingdom, SO17 1BJ*

We examine the spatio-temporal compression of energetic femtosecond laser pules within short gas filled fibers. The study is undertaken using an advanced nonlinear pulse propagation model based on a multimode generalized nonlinear Schrödinger equation that has been modified to include plasma effects. Plasma defocusing and linear propagation effects are shown to be the dominant processes within a highly dynamical mechanism that enables 100 fs pulses to be compressed into the few-cycle regime after <50 mm of propagation. Once the mechanism has been introduced, parameter spaces are explored and compressor designs suitable for performing high-field experiments in-situ are presented. We finish by showing how these designs may be extended to novel wavelengths and driving pulses delivered by state of the art high repetition rate lasers.

PACS numbers: 42.65.Re, 52.38.Hb

I. INTRODUCTION

Since the advent of chirped pulse amplification (CPA) [1] tabletop laser systems capable of surpassing terawatt peak powers have become commonplace, allowing the study of high field phenomena to flourish. Despite these advancements a constant demand remains for increased peak powers, higher repetition rates and access to novel wavelengths from the mid-infrared (MIR) through to the visible (VIS) and ultraviolet (UV). In order to meet these demands additional temporal compression is desirable after CPA, as it provides a more straightforward pathway to higher peak powers than overcoming the thermal and nonlinear issues associated with running amplifiers at a high intensity.

A popular technique for temporally compressing intense pulses is allowing them to propagate through a hollow fiber filled with an atomic gas [2]. Here, self-phase modulation (SPM) occurring within the neutral gas gives rise to spectral broadening and upon exit from the fiber dispersion compensating optics can efficiently compress multi-mJ pulses into the few-cycle regime [3]. Alternatively, conditions exist where self-compression can be achieved within laser-induced filaments [4]. Experiments of this type generally involve loosely focusing pulses into a semi-infinite gas cell with peak powers higher than the critical power for self-focusing. Once a filament forms, interplay between the linear and nonlinear responses of both plasma and neutral gas have been shown to compress high-energy pulses to durations below 8 fs [5].

Although these are both powerful techniques, hollow fiber compressors are complex devices that require specialized optics and considerable space. Also, eliminating the onset of ionization becomes challenging as designs are scaled to higher pulse energies, although progress is being made with planar waveguides [6, 7]. In filamentation-based schemes the complex filament structures generated at high intensities make exploring parameter spaces challenging both experimentally and theoretically. An interesting solution is to restrict the interaction region to a short gas-filled fiber. In such a geometry self-compression of 30 fs pulses with multi-mJ energies has been demonstrated experimentally after just 25 mm of propagation [8]. An advantage of this geometry is that it allows optimized high field experiments to be performed in-situ [9, 10]; this property is becoming invaluable as the high field community continues its shift towards the MIR [11–14] and VIS/UV [15, 16] where ultra broadband optics have not been developed.

Several theoretical studies have been undertaken that explore the propagation of high energy laser pulses through short gas-filled fibers at low to moderate gas densities. Courtois *et al.* [17] build on the coupled mode equation developed by Tempea and Brabec [18] and predict the self-compression of 7 mJ 129 fs pulses to 51 fs after just 1 mm of propagation through a fiber filled with 10 mbar of helium. In the work by Wagner *et al.* [8] numerical solutions to Christov's [19] three-dimensional scalar wave equation are included in the study. The authors also compare these solutions to experiments where 2.2 mJ 30 fs pulses were compressed to 13 fs after a 25 mm fiber filled with $\simeq 5$ mbar of argon. Recently, Skobelev *et al.* [20] and Butcher *et al.* [10] predict self-compression into the few-cycle regime within gas filled fibers and capillaries. Butcher *et al.* also begin to explore this experimentally by examining the high harmonic output of such pulse compressors.

Here, we use an advanced nonlinear pulse propagation model, based around a multimode-generalized nonlinear Schrödinger equation to examine this compression mechanism in detail. We find the rapid excitation of high-order transverse spatial modes in the plasma allows for the spatio-temporal compression of pulses with full width half maximum (FWHM) durations of 100 fs into the few-cycle regime. The process is found to be highly dynamical requiring us to utilize our CPU and GPU based high performance computing resources to develop compressor designs suitable for performing high-field ex-

periments in-situ with a broad variety of modern laser sources.

The structure of this article is as follows: in sections II and III we introduce our model and describe its computational implementation and performance, and then in sections IV, V and VI we present numerical simulations and discuss the physical processes responsible for the spatio-temporal compression. Within these simulations we study the impact of adjusting the launched pulse energy, pulse duration, central wavelength, gas parameters and fiber design. We include cases where experiments may be performed with laser systems based on titanium sapphire gain media, high repetition-rate systems using rare-earth doped fibers, up-converted sources and systems that use optical parametric chirped pulse amplification (OPCPA) or novel gain media to access the MIR. We finish by presenting some conclusions and an outlook in section VII.

II. MM-GNLSE WITH PLASMA

We will first review the formulation of a multimode generalized nonlinear Schrödinger equation (MM-GNLSE) that has been modified to take into account plasma effects [21–23]. We begin by decomposing the electromagnetic (EM) field into its transverse spatial modes and thus write the electric component as

$$\mathbf{E}(\mathbf{x},t) = \sum_m \int d\omega \frac{1}{2}\frac{\mathbf{F}_m(x,y,\omega)}{N_m(\omega)} \times e^{i\beta_m(\omega)z} A_m(z,\omega)e^{-i\omega t} + c.c.. \quad (1)$$

Here, A_m is a complex modal pulse envelope, $\mathbf{F}_m$ is a transverse spatial mode function, β_m is a modal propagation constant, N_m is a normalization factor selected such that A_m has units of pulse power and the summation extends over all M modes. Throughout this article bold typefaces represent vectorial quantities and $\mathbf{x}$ denotes the spatial coordinate (x,y,z). Following Kolesik and Moloney [24] such a decomposition allows for Maxwells equations to be transformed into a z-propagated coupled mode equation [21] of the form

$$\frac{\partial A_m(z,\omega)}{\partial z} = \frac{1}{4N_m(\omega)} \int dxdy \mathbf{F}^*_m(x,y,\omega)e^{-i\beta_m(\omega)z} \times [i\omega\mathbf{P}_{NL}(\mathbf{x},\omega) - \mathbf{j}(\mathbf{x},\omega)]. \quad (2)$$

The nonlinear polarization of the propagation medium is included through $\mathbf{P}_{NL}$, and any plasma effects that manifest at high laser intensities are introduced by the current density term $\mathbf{j}$. In deriving Eq. (2) the forward and backward propagating parts of the EM field are separated, and it is assumed that the backward propagating field is sufficiently weak to not contribute towards $\mathbf{P}_{NL}$ or $\mathbf{j}$. This assumption is justified in all but the most exotic materials and places no restrictions on the total possible bandwidth of a pulse.

We now specialize Eq. (2) to the geometry of interest: a hollow waveguide, whose core is filled with an atomic gas. In such a situation $\mathbf{P}_{NL}$ is well approximated in the temporal domain by $\varepsilon_0\chi^{(3)}_{gas}\mathbf{E}(\mathbf{x},t)\int d\tau R(t-\tau)|\mathbf{E}(\mathbf{x},t)|^2$ where ε_0 is the vacuum permittivity and $\chi^{(3)}_{gas}$ is the third order susceptibility of the neutral gas. As we are limiting our study to atomic gases, it is adequate here to replace the time response function R with a delta function. This is in contrast to short pulse propagation in molecular and solid media where slow Raman transitions are significant. Following the substitution of $\mathbf{P}_{NL}$ into Eq. (2), the frequency dependence of the mode functions and corresponding normalization conditions are neglected. These are instead included through the emerging overlap integrals, and an additional coefficient is added to describe neutral gas self-steepening [25]. We thus obtain the first two terms in our MM-GNLSE model. The first of these, $D\{A_m\}$, describes dispersion (material, intermodal, etc.) to the X^{th} order, and includes losses through the imaginary part of the propagation constant. Note that in the following expression for $D\{A_m\}$ a transformation is included to switch to a reference frame that moves at the group velocity of the fundamental mode:

$$D\{A_m(z,t)\} = i(\beta^{(0)}_m - \beta^{(0)}_0)A_m(z,t) - (\beta^{(1)}_m - \beta^{(1)}_0)\frac{\partial}{\partial t}A_m(z,t) + i\sum_{X\geq 2}\frac{\beta^{(X)}_m}{X!}\left(i\frac{\partial}{\partial t}\right)^X A_m(z,t). \quad (3)$$

The second term in the MM-GNLSE, $N\{A_{jkl}\}$, models effects resulting from the nonlinear response of the neutral gas, and is given by

$$N\{A_{jkl}(z,t)\} = i\frac{n_2\omega_0}{c}\left(1+\frac{i}{\omega_0}\frac{\partial}{\partial t}\right) \times \sum_{jkl} S_{mjkl}A_j(z,t)A_k(z,t)A^*_l(z,t), \quad (4)$$

where n_2 is the nonlinear refractive index of the neutral gas at a particular density, c is the speed of light in the vacuum, ω_0 is a central frequency and S_{mjkl} are the transverse mode overlap integrals [21]. In deriving Eq. (4), additional terms responsible for third-harmonic generation have been dropped as they are assumed to be poorly phase matched.

Within our fiber $\mathbf{j}$ can be described in the temporal domain by

$$\frac{\partial \mathbf{j}(\mathbf{x},t)}{\partial t} = -\varepsilon_0\omega^2_{plasma}(\mathbf{x},t)\mathbf{E}(\mathbf{x},t) - \varepsilon_0 c\frac{\partial}{\partial t}\frac{\sum_q \rho_q(\mathbf{x},t)W_q(\mathbf{x},t)U_q}{|\mathbf{E}(\mathbf{x},t)|^2}\mathbf{E}(\mathbf{x},t), \quad (5)$$

where ω_{plasma} is the plasma frequency and ρ_q, W_q and U_q represent the density, ionization rate and ionization potential of the q^{th} charge state of the gas [17]. Note

that ω_{plasma} is a function of the total free-electron density $\sum_q q\rho_q$ making these terms highly nonlinear through the strong field-dependence of both ρ_q and W_q. Once introduced into Eq. (2), we can extract terms that enable plasma defocusing $P\{A\}$ and plasma induced losses $PL\{A\}$ to be included in our MM-GNLSE model. These modifications take the form

$$P\{A(z,t)\} = -\frac{i}{2}\frac{\omega_0}{c}\left(1 - \frac{i}{\omega_0}\frac{\partial}{\partial t}\right) \times \int dxdy \frac{\mathbf{F}_m^* \mathbf{E}(\mathbf{x},t)}{N_m} \frac{\omega_{plasma}^2(\mathbf{x},t)}{\omega_0^2} \quad (6)$$

and

$$PL\{A(z,t)\} = -\frac{1}{2}\int dxdy \frac{\mathbf{F}_m^* \mathbf{E}(\mathbf{x},t)}{N_m} \times \frac{\sum_q \rho_q(\mathbf{x},t) W_q(\mathbf{x},t) U_q}{|\mathbf{E}(\mathbf{x},t)|^2}. \quad (7)$$

We now collect terms and arrive at a coupled mode equation that we will refer to as the modified MM-GNLSE

$$\frac{\partial A_m(z,t)}{\partial z} = D\{A_m(z,t)\} + N\{A_{jkl}(z,t)\} + P\{A(z,t)\} + PL\{A(z,t)\}. \quad (8)$$

At field strengths and pulse durations of interest to us, we estimate the densities of successive charge states by solving the system $\frac{\partial \rho_0}{\partial t} = -W_0\rho_0$, $\frac{\partial \rho_q}{\partial t} = -W_{q-1}\rho_{q-1} - W_q\rho_q$, $\frac{\partial \rho_Q}{\partial t} = -W_{Q-1}\rho_{Q-1}$. Here Q represents the highest achievable electronic charge, and Keldysh theory is applied to calculate the ionization rates of the atomic/ionic gas [26].

The modified MM-GNLSE model has been verified by numerous experimental measurements over a large range of pulse and gas parameters. A spatio-spectral comparison is given in [22], and when propagated into the far-field the model compares well to frequency resolved optical gating (FROG) measurements.

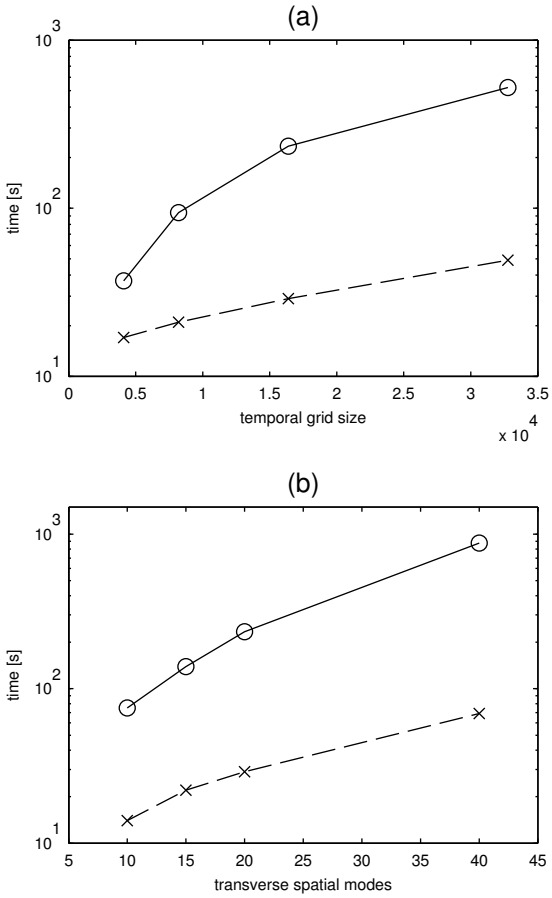

FIG. 1. (a) The time required to propagate 20 modes through a section of fiber as a function of temporal grid size using our sequential CPU (solid) and parallel GPGPU (dashed) implementations. (b) A similar performance analysis as a function of the number of transverse spatial modes included in the simulation. The pulse energy used here was 1 mJ, the FWHM duration of the Gaussian pulse envelope was 40 fs and the central wavelength was positioned at 800 nm. The fiber was 50 mm in length and the 150 μm (diameter) core was filled with 100 mbar of argon.

III. NUMERICAL IMPLEMENTATION

The algorithm used to solve the modified MM-GNLSE is a symmetrized split-step Fourier method (SSFM) [27] with error checking and adaptive step size control included via a Runge-Kutta-Fehlberg method [28]. Initial conditions are found by calculating overlap integrals between the launched laser field and the mode functions supported by the fiber. In this work we exploit the preferential coupling that exists between a linearly polarized free-space Gaussian beam and the $EH_{1,n}$ modes of a hollow dielectric fiber with a circular core. For centered launching conditions this allows us to restrict our analysis to far fewer modes, as spontaneous processes that can couple light into non-circularly symmetric modes are weak at high peak powers and over short propagation lengths [23]. In such a fiber the mode functions and complex propagation constants have approximate analytic forms [29], the normalization condition is chosen to be $N_m = [\int dxdy|F_m|^2]^{\frac{1}{2}}$ and the mode overlap integrals become $S_{mjkl} = \frac{\int dxdy F_m F_j F_k F_l}{N_m N_j N_k N_l}$.

Our simulations have been implemented in the C++ programming language, and the Eigen [30], ArrayFire (AccelerEyes) and FFTW 3 [31] libraries are called upon for linear algebra, vectorized mathematical operations and fast Fourier transforms (FFTs) respectively. When exploring large parameter spaces many instances of the code are initialized at once on our 12,000 core computing cluster, however the algorithm itself remains sequential. Additionally, we have developed an implementation that allows sections of the algorithm to be executed in parallel on general purpose graphical processing units (GPG-

PUs). Figure 1 illustrates the time required to complete a 50 mm propagation as a function of the temporal grid size (a) and number of transverse spatial modes (b). All other parameters are fixed and sequential calculations are performed on a single 2.4 GHz Westmere core (Intel corporation) and the parallel version utilizes a Tesla M2050 GPGPU (NVIDIA corporation) with 448 CUDA cores. The performance increases seen when working with large temporal grids or many modes are attributed to our efficient parallel evaluation of the computationally complex nonlinear operator. The execution times shown in Fig. 1 are representative of those achieved in the following numerical simulations.

IV. NUMERICAL SIMULATIONS AT 800 NM

Oscillator-amplifier systems using a bulk Ti:sapphire gain media are a relatively mature technology and are widely available commercially. Short pulse variants typically have pulse durations of 25 - 50 fs, central wavelengths of 800 nm and depending on repetition rate pulse energies between 100 μJ and 10 mJ. This section describes the application of the modified MM-GNLSE to study the spatio-temporal evolution of such pulses through short sections of gas filled fiber.

A. An initial simulation and physical mechanisms

For our initial simulation 20 modes were selected and the launch parameters were adjusted to achieve optimal coupling into the fundamental $EH_{1,1}$ mode [32]. The central wavelength of the driving pulse was positioned at 800 nm, the pulse energy was limited to 800 μJ and the FWHM duration of the Gaussian envelope was 40 fs. The fused-silica fiber design used here was 50 mm in length with a hollow core diameter of 150 μm and was assumed to be homogeneously filled with 100 mbar of argon. These parameters are consistent with those used in our experimental work [10, 22].

The results of such a simulation are shown in Fig. 2. The envelopes of the first 5 modes at the exit of the fiber are presented in (a). We have restricted the number of modes included in this figure for clarity only. At launch (see inset) 98.1 % of the power is contained in the fundamental mode, and as the pulse propagates higher order modes are rapidly excited via the nonlinear source term $P\{A(z,t)\}$, Eq. (6).

This rapid spatial redistribution of power gives rise to some interesting temporal behaviour. The strong nonlinear field dependence of the photoionization process leads to steps in the intensity dependent refractive index. These steps are not only responsible for extensive spectral broadening via SPM but their positioning acts as a gate for the excitation of temporally compressed higher order modes. In Fig. 2(a) the initial refractive index step occurs just before the peak of the fundamental mode, causing its trailing edge to steepen as power is defocussed by the plasma into (predominantly) the first higher order mode. If the power of the $EH_{1,2}$ mode becomes sufficiently high the process can repeat, resulting in a spread of temporally compressed envelopes trailing the remnants of the fundamental mode. This qualitative description based on analyzing the complex modal envelopes becomes less clear once several modes reach an equivalent power. In this case it is more appropriate to study the full spatio-temporal field (Fig. 2(b)). The dominant features at $t > 0$ arise when several of the bright higher order modes overlap such that they are in phase. In this particular example at $t \simeq 50$ fs the on-

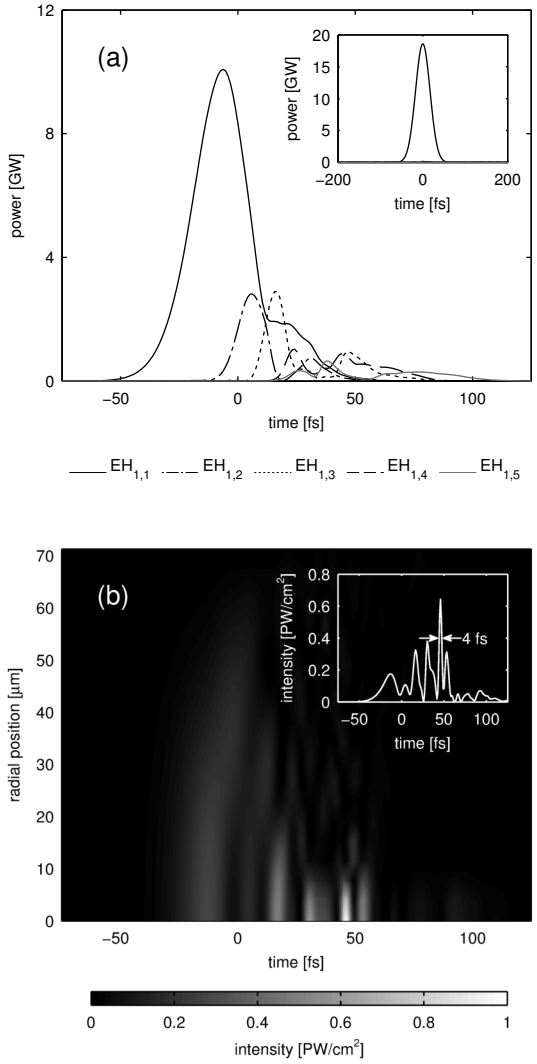

FIG. 2. (a) The modal pulse envelopes at the exit of a 50 mm section of hollow fiber filled with 100 mbar of argon. (inset) The envelopes of the 40 fs pulse at the launch. (b) The spatio-temporal field at the output constructed from these envelopes and their transverse spatial mode functions. The most intense feature within the on-axis field (see inset) is compressed to a FWHM duration of 4 fs.

axis FWHM duration (see the inset) is reduced to 4 fs, giving an order of magnitude of temporal compression after just 50 mm of propagation. Additionally, Fig. 2(b) shows the spatial half width half maximum (HWHM) of the pulse reducing to $\simeq 5$ μm. It is an interesting feature of the waveguide geometry that plasma defocusing can in fact drive spatial compression at peak powers well below the critical power for neutral gas self-focusing. The key aspects of this mechanism can be developed using a simplified 5 mode continuous wave (CW) model with a 3-dimensional Gaussian distribution of free-electrons centered at $\mathbf{x} = (0, 0, 0)$ (See Fig. 3 for the dimensions of this scattering object). Firstly, optical power is defocused from the fundamental mode (spatial HWHM $\simeq 40$ μm) into the higher order modes, and secondly the intermodal dispersion characteristics of the fiber produce an intense region where the beat lengths of the three highest order modes are close to overlapping, reducing the spatial HWHM to $\simeq 20$ μm. In contrast to the CW case where the intensity increase can be attributed to spatial compression alone, the addition of temporal compression in the modified MM-GNLSE solution (Fig 2(b)) makes the radial intensity variation more pronounced.

Returning to our initial simulation the spatio-temporal reshaping achieved within the fiber is highly dynamical. Figure 4 demonstrates the spatial HWHM (a), on-axis FWHM duration (b) and on-axis peak intensity (c) as a function of the z-coordinate. When constructing these plots and throughout the rest of this article we take the convention of analyzing the most intense feature within the pulse at each z-position. Although this leads to discontinuities we consider it to be the most appropriate way to present our data with high field applications in mind. Much of this dynamic behaviour is in fact driven by linear propagation effects. Intermodal dispersion causes the relative phases of the modes to slip, modulating the spatio-temporal field calculated from the coherent sum involving all complex envelopes and mode functions, Eq. (1). Also, as we are coupling a considerable quantity of power into high order modes, their large loss influences the distance over which a short pulse can be maintained with a high intensity. Figure 4(a) shows the spatial dynamics arising from this mode coupling, while Fig. 4(b) shows the corresponding temporal behaviour. Correlations between these indicate simultaneous spatio-temporal compression as in Fig. 2(b). Increases in intensity are also observed within the fiber (Fig. 4(c)). It has been suggested that by analysing the high harmonic spectrum in the far-field these could be verified experimentally [33], and in fact we have recently demonstrated a similar approach in our experiments [10]. Figure 4 also highlights that regions exist within the fiber

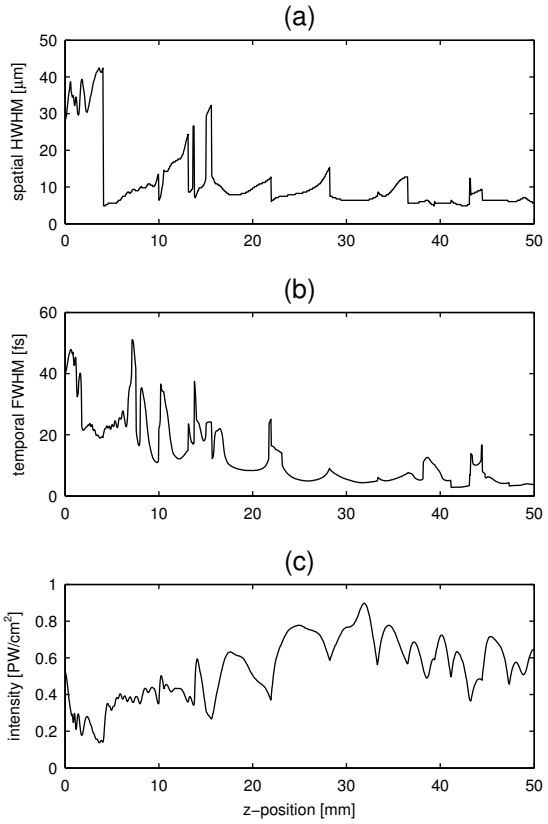

FIG. 4. The spatial HWHM (a), on-axis FWHM duration (b) and on-axis intensity as a function of propagation distance. The discontinuities result from our convention of analyzing the most intense feature within the complicated pulse structure.

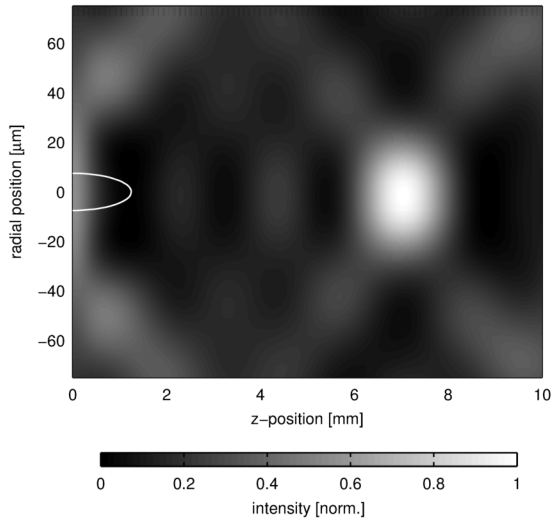

FIG. 3. The results of a simple 5 mode CW model used to examine the spatial reshaping mechanism occurring within the fiber. Defocussing by the 3-dimensional Gaussian distribution of free-electrons (whose spatial FWHM and HWHM dimensions are illustrated by the solid curve) and subsequent mode beating produces the spatially compressed feature at z = 7 mm.

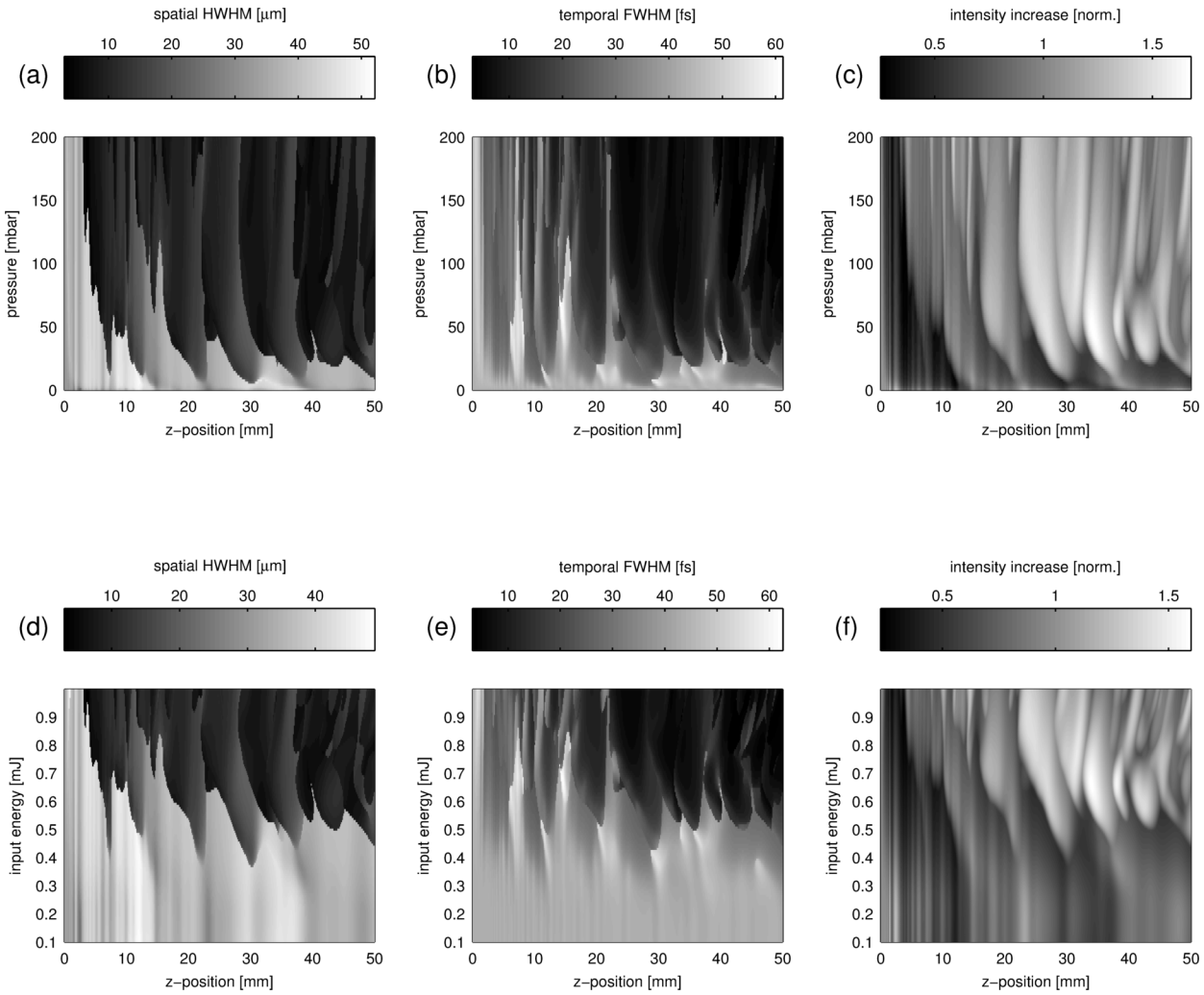

FIG. 5. The (a), on-axis FWHM duration (b) and on-axis intensity increase as a function of propagation distance and argon pressure within the fiber. The plots (d), (e) and (f) highlight these properties as a function of the input pulse energy. All other parameters used for these simulations are identical to our initial simulation. These plots enable us to optimise a compressor design to a particular laser system.

where a high intensity pulse is maintained with a few-cycle duration over several mm opening up the possibility of generating isolated attosecond bursts of extreme ultraviolet (XUV) radiation [34]. An attosecond source of this type has has been studied theoretically in the filament geometry [35] but the hollow fiber approach is an attractive alternative due to the extensive body of work that exists regarding high harmonic generation (HHG) in short gas filled fibers [36, 37].

B. Alternative parameter regimes

We now explore the effectiveness of the compression mechanism across the pressure and input pulse energy parameter space. This will allow us to gain a deeper understanding of the physics, generate datasets from which compressors can be designed and expand the potential applications of this pulse compression technique. Figure 5(a) and (b) show the spatial HWHM and on-axis FWHM duration as a function of the z-coordinate and argon pressure. These simulations demonstrate the importance of generating a high free-electron density when highly multimode propagation is the desired outcome. Figures 5(d) and (e) show the same quantities as a function of the z-coordinate and input pulse energy. Again, the plots demonstrate the importance of a high free-electron density but also show the nonlinearity of the photoionization process itself, producing distinct boundaries within which spatio-temporal compression is predicted. These datasets further highlight the relationship between spatial and temporal compression. These results suggest that whenever bright, nonlinearly excited higher order modes are observed in the far-field of an experiment then temporally compressed pulses are likely to exist within the fiber, at least in the limit of pressures

where material dispersion has a negligible effect. The remaining plots in Fig. 5 show the increase in on-axis intensity as a function of z-coordinate, argon pressure (c) and input energy (f). We find significant parameter regimes where intensities increase by up to 1.6-fold, and in these regions the compressed pulse can contain as much as 20% of the launched energy. However, not all parameters where spatio-temporal compression is observed also show an increase in intensity. This is predominantly due to intermodal dispersion, but linear and nonlinear losses also have an impact. Here, this is relevant towards the exit of the fiber and at high pulse energies where multiple sequential ionizations occur. This complex dynamic behaviour prevents a simple prediction as to where intensity spikes might occur, and instead a numerical approach such as ours here is required for the exact parameter set of interest. From these simulations we suggest that an interesting compressor design suitable for performing in-situ high field experiments involves launching 800μJ pulses into a 35 mm long fiber filled with 100 mbar of argon. In this case high intensity 4 fs pulses are predicted near to the exit.

V. NUMERICAL SIMULATIONS AT 1050 NM WITH LOW ENERGY LONG PULSES

An interesting and timely application for this technique is the compression of 100 μJ few-hundred fs pulses delivered by compact ytterbium-doped fiber CPA systems. The high repetition rates achievable from such architectures are of interest to the high field community because of the enhancements in signal yield they could bring and new opportunities they could open up, such as performing metrology with XUV frequency combs [16]. Our simulations in this parameter regime may also be applicable to pulses delivered by high repetition rate regenerative amplifiers, thin-disk lasers, slab amplifiers and certain coherent combination arrangements.

Activating the compression mechanism presented in section IV for initial conditions of this type is not straightforward because of the much lower peak powers delivered by such driving lasers. Several alterations are needed in order to produce a large step in refractive index by gas ionization. First, the gas must be exchanged for one with lower ionization potentials. For these simulations we have chosen to work with xenon, but more exotic gaseous species may prove to be an interesting alternative if their nonlinear polarizations and ionization rates can be described correctly. This change is not enough to produce high free electron densities, so the fiber must also be switched for one with a smaller core diameter to increase the field strength. In these simulations we work with 20 modes and launch Gaussian pulses with an energy of 100 μJ, a FWHM duration of 275 fs and a central wavelength of 1050 nm. The fiber section used here was 50 mm long and the core diameter was varied between 40 μm and 60 μm. The xenon pressure was fixed at 200 mbar to maximise the potential for generating a high free electron density. The results of these simulations are given in Fig. 6. Figure 6(a) and (b) show changes in the spatial HWHM and the on-axis FWHM duration as a function of the z-coordinate and the fibers core diameter. In order to observe extensive coupling into high order modes and the temporal compression we have shown this to herald, core diameters must be kept below 45 μm for the chosen pulse energy. Within such fibers 275 fs pulses can be compressed to 69 fs after 5 mm of propagation.

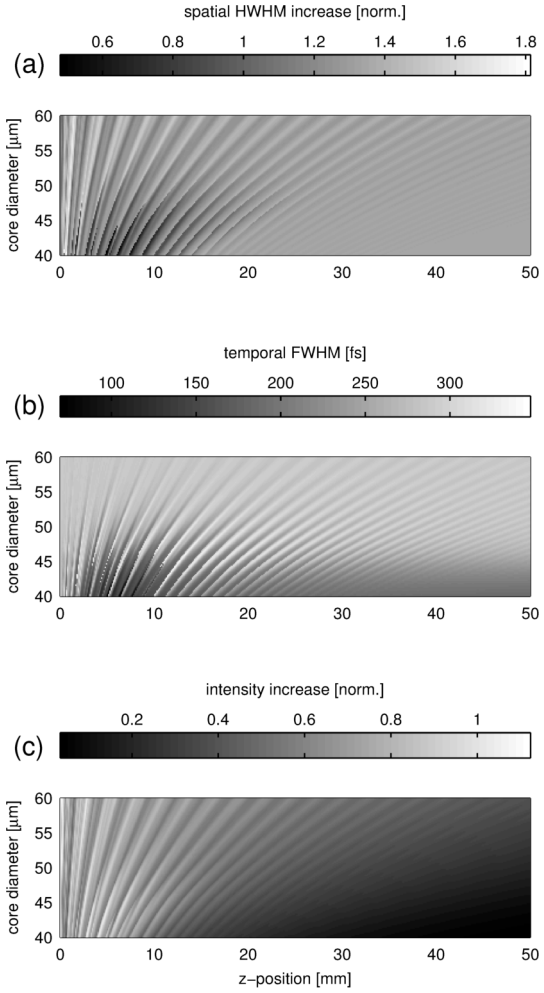

FIG. 6. The change in spatial HWHM (a), on-axis FWHM duration (b) and intensity increase (c) as a function of z-coordinate and core diameter. The launched FWHM duration is 275 fs and this is compressed to a minimum of 69 fs after 5 mm of propagation.

As we reduce the size of the core the propagation becomes increasingly dynamic early in the fiber. The pulse then undergoes a stabilization, maintaining a FWHM duration of 165 fs throughout the remainder of the propagation. In order to explain the physical origins of these two regions it is helpful to study the modal propagation constants over a broad range of core diameters. Figure

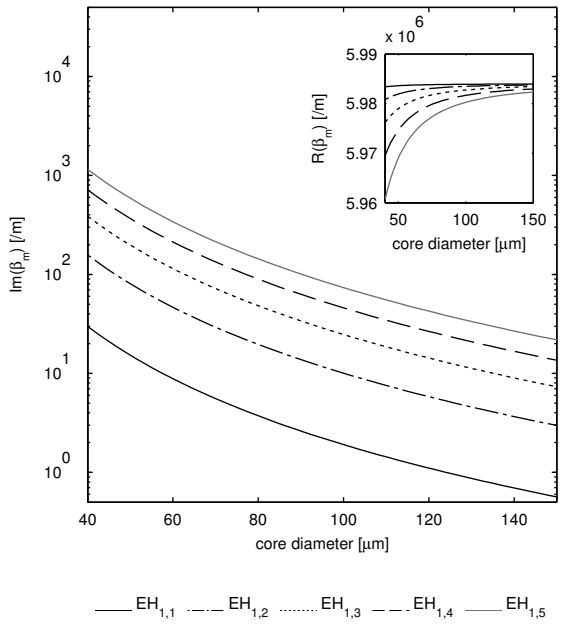

FIG. 7. The real (inset) and imaginary part of the propagation constant as a function of core diameter. The data plotted is for the first 5 modes at a wavelength of 1050 nm.

7 shows the real (inset) and imaginary parts of β_m as a function of core diameter for the 5 lowest order modes. The increase in separation between real parts at small core diameters leads to short characteristic beat lengths and the strong interference patterns seen in Fig. 6. When we compare the imaginary parts of these and our earlier simulations a difference of 2 orders of magnitude is observed, and such a large increase in linear loss causes the apparent stabilisation of the pulse after $\simeq 20$ mm of propagation. The lack of significant enhancement in on-axis peak intensity (Fig. 6(c)) is due to these large losses, and in this region the pulse is contained predominately within the steepened fundamental mode.

A design that will compress 100μJ pulses with 275 fs FWHM durations to 69 fs would consist of a 5 mm xenon filled fiber with a 40 μm core diameter. Many applications will find a 4 fold reduction in pulse length (while maintaining a high intensity) helpful, but the underlying mechanism should allow access to far shorter durations and large intensity increases if the linear losses can be adequately controlled. In future theoretical and experimental work we will achieve this by incorporating low-loss microstructured fibers [38–40] into our designs.

VI. NUMERICAL SIMULATIONS FROM THE VIS TO MIR

For our final set of simulations we explore how the pump wavelength effects spatio-temporal compression and peak intensities within gas filled fibers. This is of interest because of current shifts in the high field community away from the near infrared and towards VIS and MIR wavelengths. High energy pulses throughout this region are being made available by efficient wavelength conversion modules (harmonic generation and optical parametric amplifiers) and laser systems utilizing the OPCPA technique and novel gain media.

For this set of simulations we have reverted to a fiber with a 150 μm core diameter and 50 mm length. The fiber was filled with 100 mbar of argon, and 20 modes were launched under conditions that gave an optimal coupling into the fundamental mode. The pulse energy used was 1.5 mJ, the FWHM duration was 100 fs and the wavelength varied between 500 nm and 2000 nm. The results are shown in Fig. 8. The format here is similar to previous simulations, (a) shows the spatial HWHM, (b) the on-axis FWHM duration and (c) the on-axis intensity increase as a function of z-coordinate and the central wavelength. Again we see a clear correlation between the excitation of high order modes and temporal compression. The parameter space where spatio-temporal compression can be achieved is extensive, and recalling that a three-cycle pulse positioned at 2000 nm has an approximate duration of 20 fs, pulses containing a single optical cycle may be synthesized at MIR wavelengths.

Similar to the approach discussed in section V, changing the wavelength while keeping the fiber diameter constant impacts the intermodal dispersion and linear losses. Figure 8(d) shows how the real (inset) and imaginary parts of β_m change as a function of wavelength for the first 5 modes. The order of magnitude change in loss across the simulations begins to limit spatio-temporal compression and intensity increases (Fig. 8(c)) over long propagation lengths at MIR wavelengths. If we restrict our analysis to shorter fibers, Fig. 8(e) shows the spatio-temporal field of a 1500 nm pulse after 16 mm of propagation. Such a design enables a 100 fs Gaussian pulse to be modulated into a pulse whose most intense feature contains just 2 optical cycles.

VII. CONCLUSION

We have reviewed the derivation of a modified MM-GNLSE capable of describing the propagation of intense laser pulses through gas filled fibers. This model includes dispersion and losses associated with waveguiding, neutral gas nonlinearities, plasma induced effects and self-steepening. An efficient numerical implementation was developed and implemented on a large computing cluster allowing us to locate parameter spaces where many-cycle pulses can be self-compressed to few-cycle durations. We focus on parameters that are of interest to the high field physics community, and suggest that such experiments can be performed in-situ with pulse compression.

The pulse compression technique described here relies on the nonlinear ionization of neutral gasses to gener-

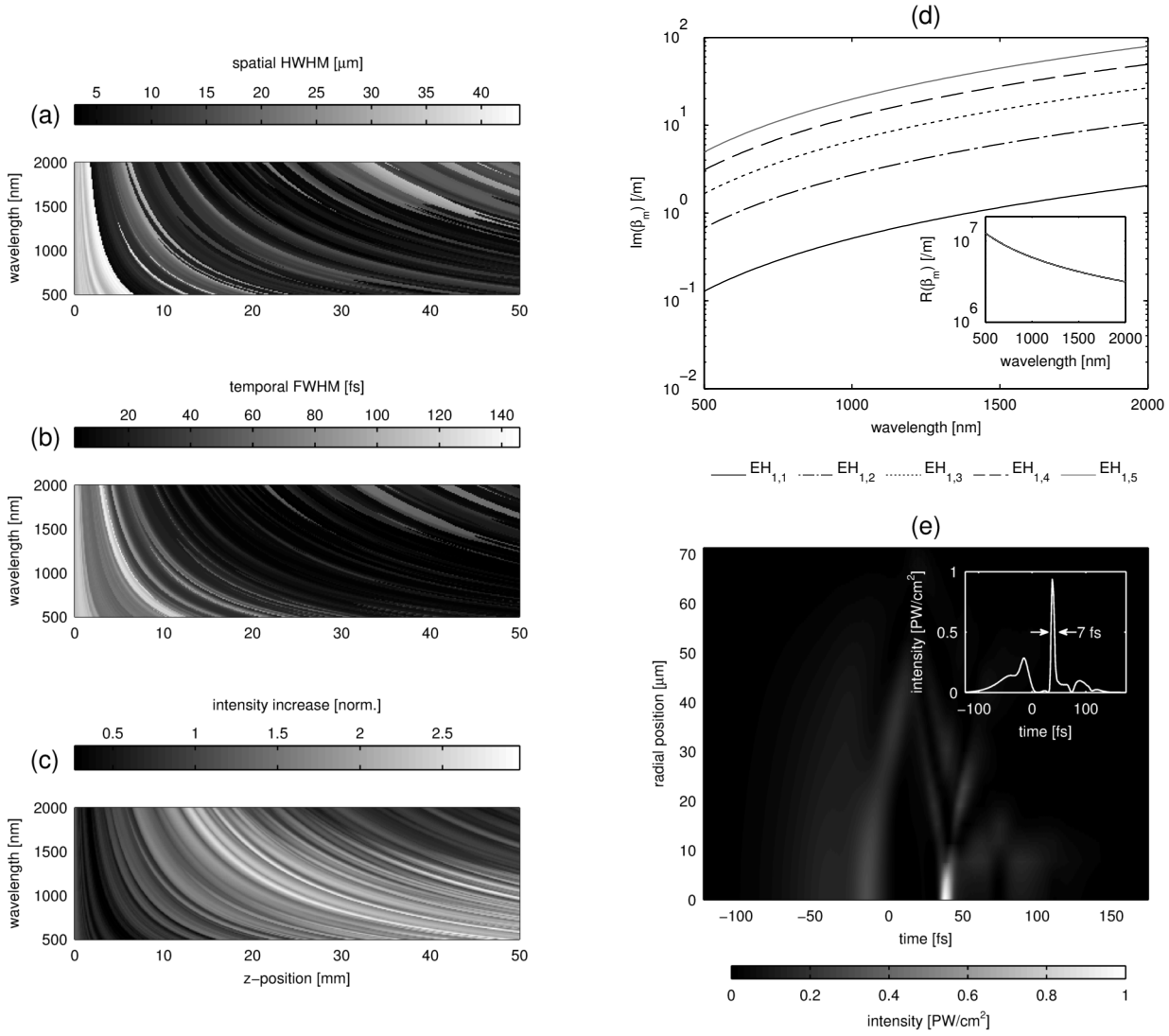

FIG. 8. The spatial HWHM (a), on-axis FWHM duration (b) and on-axis peak intensity increase (c) as a function of propagation distance and the central wavelength from the VIS to MIR. (d) The real (inset) and imaginary part of the propagation constant as a function of central wavelength. Here the fiber has a core diameter of 150 μm. On such a scale it is difficult to differentiate between the real parts of the individual modes but their separation increases with wavelength. (e) The full spatio-temporal field of a 1500 nm pulse after 16 mm of propagation. Close to the optical axis (inset) the pulse is compressed to a 7 fs FWHM duration.

ate high free-electron densities. Plasma defocusing causes a considerable quantity of power to be coupled into temporally compressed high order modes, and linear propagation effects lead to interesting dynamic behaviour. For example 40 fs pulses are compressed to 4 fs after 35 mm of propagation through a fiber filled with 100 mbar of argon. We also explored the pressure and pulse energy parameter space and found that when bright, nonlinearly excited high order modes are observed in the far-field temporal compression is likely to have taken place.

In the final two sections we moved away from studying pulses delivered from Ti:sapphire based amplifiers and towards high repetition rate sources and novel wavelengths between the VIS and MIR. We show the pulse compression mechanism can be extended to both of these regimes, however the high loss of the fiber can become a limiting factor to achieving high peak powers. In future work we wish to address this by replacing the simple hollow core fiber with a microstructured fiber, where losses can be three orders of magnitude lower. With such fibers we expect to achieve high intensity, few-cycle pulses suitable for in-situ high field experiments at a repetition rates between 10 kHz and 1 MHz.

VIII. ACKNOWLEDGEMENTS

We acknowledge the Engineering and Physical Sciences Research Council (EPSRC), the University of Southampton and the e-Infrastructure South consortium for providing a studentship and extensive long-term access to the Iridis supercomputer.

[1] P. Maine, D. Strickland, P. Bado, M. Pessot, and G. Mourou, IEEE Journal of Quantum Electronics **24**, 398 (1988).
[2] M. Nisoli, S. De Silvestri, and O. Svelto, Applied Physics Letters **68**, 2793 (1996).
[3] S. Bohman, A. Suda, T. Kanai, S. Yamaguchi, and K. Midorikawa, Optics Letters **35**, 1887 (2010).
[4] A. Couairon and A. Mysyrowicz, Physics Reports **441**, 47 (2007).
[5] G. Stibenz, N. Zhavoronkov, and G. Steinmeyer, Optics Letters **31**, 274 (2006).
[6] M. Nurhuda, A. Suda, S. Bohman, S. Yamaguchi, and K. Midorikawa, Physical Review Letters **97**, 153902 (2006).
[7] S. Akturk, C. L. Arnold, B. Zhou, and A. Mysyrowicz, Optics Letters **34**, 1462 (2009).
[8] N. Wagner, E. Gibson, T. Popmintchev, I. Christov, M. Murnane, and H. Kapteyn, Physical Review Letters **93**, 173902 (2004).
[9] P. Arpin, T. Popmintchev, N. Wagner, a. Lytle, O. Cohen, H. Kapteyn, and M. Murnane, Physical Review Letters **103**, 1 (2009).
[10] T. J. Butcher, P. N. Anderson, R. T. Chapman, P. Horak, J. G. Frey, and W. S. Brocklesby, Physical Review A **87**, 043822 (2013).
[11] R. Torres, T. Siegel, L. Brugnera, I. Procino, J. G. Underwood, C. Altucci, R. Velotta, E. Springate, C. Froud, I. C. E. Turcu, S. Patchkovskii, M. Y. Ivanov, O. Smirnova, and J. P. Marangos, Physical Review A **81**, 051802 (2010).
[12] B. Shim, S. E. Schrauth, and A. L. Gaeta, Optics Express **19**, 9118 (2011).
[13] T. Popmintchev, M.-C. Chen, D. Popmintchev, P. Arpin, S. Brown, S. Alisauskas, G. Andriukaitis, T. Balciunas, O. D. Mücke, A. Pugzlys, A. Baltuska, B. Shim, S. E. Schrauth, A. Gaeta, C. Hernández-García, L. Plaja, A. Becker, A. Jaron-Becker, M. M. Murnane, and H. C. Kapteyn, Science **336**, 1287 (2012).
[14] J. Andreasen and M. Kolesik, Physical Review E **87**, 053303 (2013).
[15] E. L. Falcao-Filho, C.-J. Lai, K.-H. Hong, V.-M. Gkortsas, S.-W. Huang, L.-J. Chen, and F. X. Kartner, Applied Physics Letters **97**, 061107 (2010).
[16] B. Bernhardt, A. Ozawa, A. Vernaleken, I. Pupeza, J. Kaster, Y. Kobayashi, R. Holzwarth, E. Fill, F. Krausz, T. W. Hänsch, and T. Udem, Optics Letters **37**, 503 (2012).
[17] C. Courtois, A. Couairon, B. Cros, J. R. Marques, and G. Matthieussent, Physics of Plasmas **8**, 3445 (2001).
[18] G. Tempea and T. Brabec, Optics Letters **23**, 762 (1998).
[19] I. P. Christov, Journal of the Optical Society of America B **18**, 1877 (2001).
[20] S. A. Skobelev, A. V. Kim, and O. Willi, Physical Review Letters **108**, 123904 (2012).
[21] F. Poletti and P. Horak, Journal of the Optical Society of America B **25**, 1645 (2008).
[22] R. T. Chapman, T. J. Butcher, P. Horak, F. Poletti, J. G. Frey, and W. S. Brocklesby, Optics Express **18**, 13279 (2010).
[23] P. Horak and F. Poletti, in *Recent Progress in Optical Fiber Research*, edited by M. Yasin, S. W. Harun, and H. Arof (Intech, 2012) pp. 3–25.
[24] M. Kolesik and J. V. Moloney, Physical Review E **70**, 36604 (2004).
[25] J. M. Dudley, G. Genty, and S. Coen, Reviews of Modern Physics **78**, 1135 (2006).
[26] V. S. Popov, Physics-Uspekhi **47**, 855 (2004).
[27] G. P. Agrawal, *Nonlinear Fiber Optics*, Optics and Photonics (Academic Press, 2007).
[28] W. H. Press, S. A. Teukolsky, W. T. Vetterling, and B. P. Flannery, *Numerical Recipes 3rd Edition: The Art of Scientific Computing*, Numerical Recipes: The Art of Scientific Computing (Cambridge University Press, 2007).
[29] E. A. J. Marcatili and R. A. Schmeltzer, The Bell Sysyem Technical Journal **43**, 1783 (1964).
[30] G. Guennebaud and B. Jacob, "Eigen v3," http://eigen.tuxfamily.org (2010).
[31] M. Frigo and S. Johnson, in *Proceedings of the IEEE*, Vol. 93 (2005) pp. 216–231.
[32] R. K. Nubling and J. A. Harrington, Optical Engineering **37**, 2454 (1998).
[33] M. Gaarde and A. Couairon, Physical Review Letters **103**, 043901 (2009).
[34] P. Corkum and F. Krausz, Nature Physics **3**, 381 (2007).
[35] H. S. Chakraborty, M. B. Gaarde, and A. Couairon, Optics Letters **31**, 3662 (2006).
[36] A. Rundquist, C. Durfee III, Z. Chang, C. Herne, S. Backus, M. Murnane, and H. Kapteyn, Science **280**, 1412 (1998).
[37] O. H. Heckl, C. R. E. Baer, C. Kränkel, S. V. Marchese, F. Schapper, M. Holler, T. Südmeyer, J. S. Robinson, J. W. G. Tisch, F. Couny, P. Light, F. Benabid, and U. Keller, Applied Physics B **97**, 369 (2009).
[38] R. Cregan, B. Mangan, J. Knight, T. Birks, P. S. J. Russell, P. Roberts, and D. Allan, Science **285**, 1537 (1999).
[39] F. Couny, F. Benabid, and P. Light, Optics Letters **31**, 3574 (2006).
[40] F. Gérôme, R. Jamier, J.-L. Auguste, G. Humbert, and J.-M. Blondy, Optics Letters **35**, 1157 (2010).